Electronic Supplementary Information

Cation-exchange-assisted formation of NiS/SnS_2 porous nanowalls with ultrahigh energy density for battery-supercapacitor hybrid devices

Shundong Guan,[a,b] Xiuli Fu,*[a] Bo Zhang,[a] Ming Lei[a] and Zhijian Peng*[b]

[a] State Key Laboratory of Information Photonics and Optical Communications, and School of Science, Beijing University of Posts and Telecommunications, Beijing 100876, P. R. China

[b] School of Science, China University of Geosciences, Beijing 100083, P. R. China

*[a] E-mail: xiulifu@bupt.edu.cn (X Fu); Tel: 86-10-62282242; Fax: 86-10-62282242;

*[b] E-mail: pengzhijian@cugb.edu.cn (Z Peng); Tel: 86-10-82320255; Fax: 86-10-82322624;

Financial support from the National Natural Science Foundation of China (grant nos. 11674035), and BUPT Excellent Ph.D. Students Foundation (grant no. CX2018214) is gratefully acknowledged.

Supplementary Figures

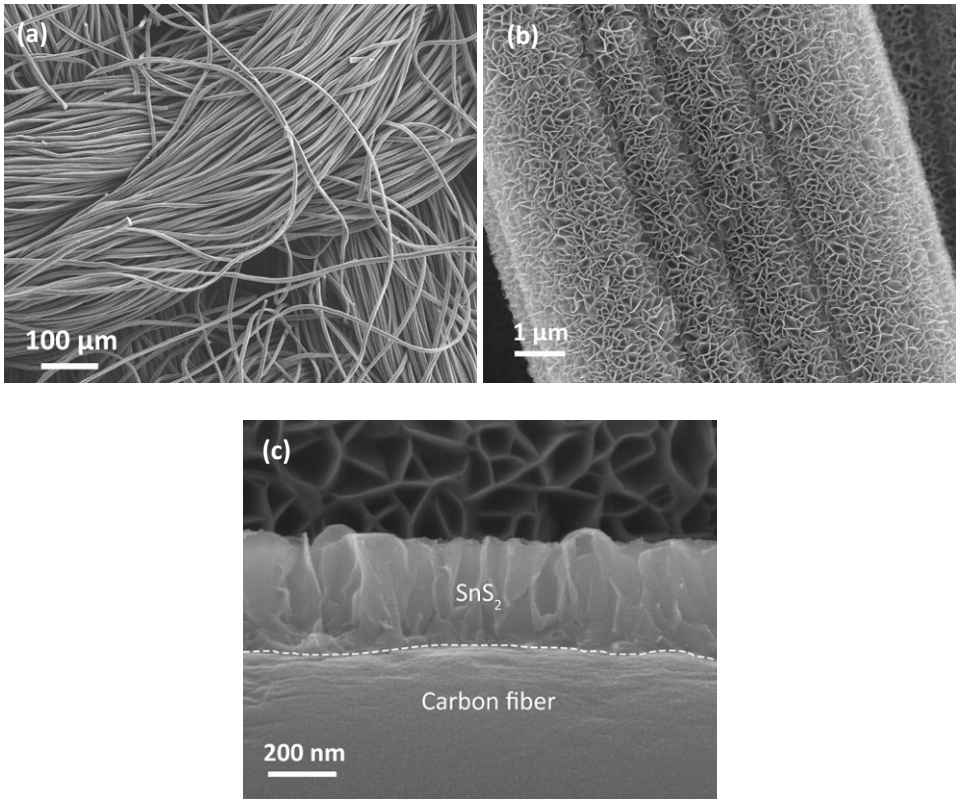

Fig. S1 Typical surface SEM images of bare CC **(a)** and SnS_2@CC **(b)**, respectively. SEM image of a fractured SnS_2@CC **(c)**.

From **Fig. S1a**, it can be seen that CC shows a braided structure, consisting of many oriented carbon fibers with an average diameter of approximately 10 μm. As is seen in **Fig. S1b** and **1c**, the SnS_2 nanosheets directly and vertically grew on the surface of the carbon fibers in CC, which have an average height of approximately 300 nm.

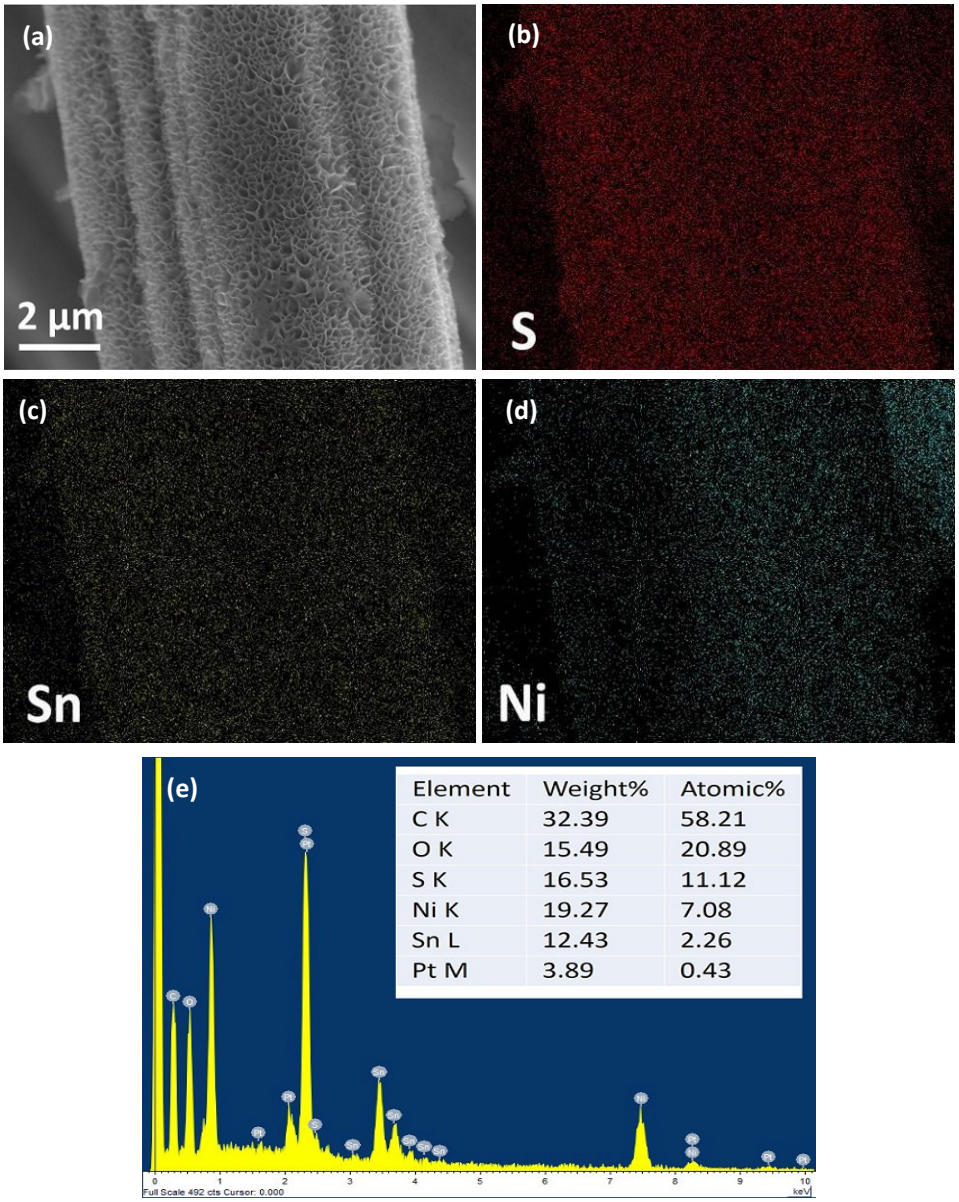

Fig. S2 Typical SEM-EDX results for NiS/SnS_2@CC synthesized with a reaction time of 6 h. **(a)** SEM image and the corresponding mapping images of **(b)** S, **(c)** Sn, and **(d)** Ni. **(e)** EDX spectrum and the corresponding elemental contents.

From the SEM-EDX mapping images (**Fig. S2a-2d**), it can be seen that the S, Sn, and Ni atoms are uniformly distributing on the whole surface of carbon fibers, indicating that NiS evenly grew on the surface of SnS_2 template. The contents of S, Sn, and Ni atoms present a relationship of S ≈ 2Sn + Ni, which is well matching with the stoichiometry of SnS_2 + NiS (**Fig. S2e**). In addition, the molar content of NiS in the NiS/SnS_2 composite can be determined as approximately 75.8% (**Fig. S2e**).

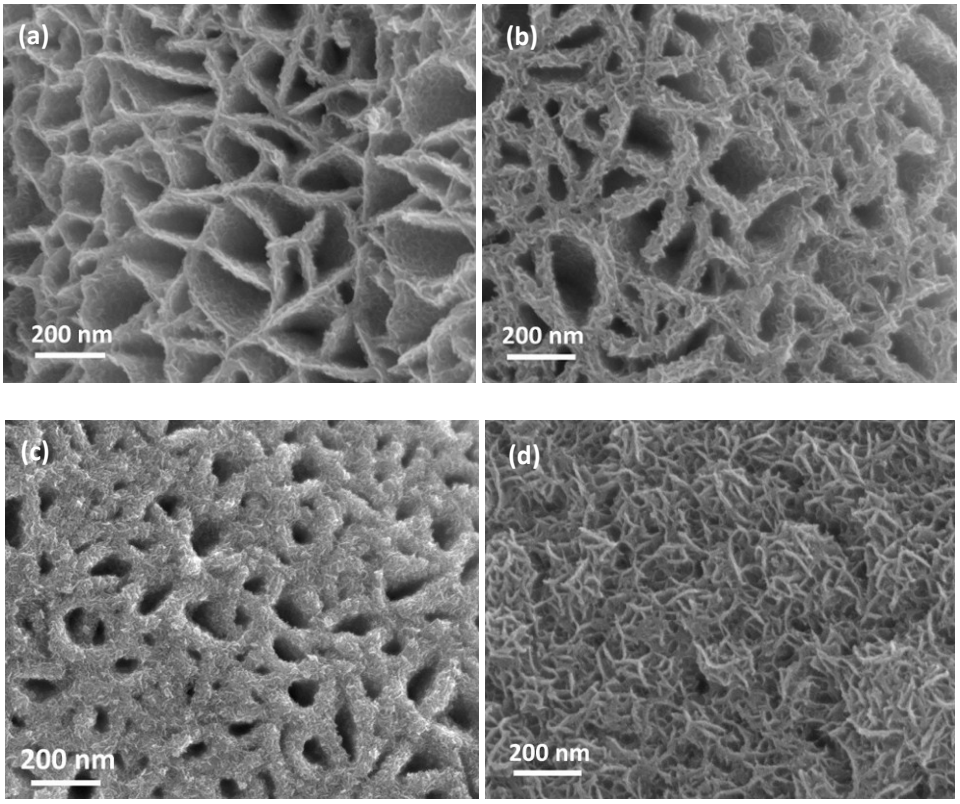

Fig. S3 SEM images of NiS/SnS_2@CC synthesized with different cation-exchange reaction times: **(a)** 4, **(b)** 8, **(c)** 10, and **(d)** 12 h.

The morphology of NiS/SnS_2 changes with the cation-exchange reaction time. With a reaction time of 4 h, only small amount of SnS_2 was replaced by NiS and the sheet-like structure of the precursor almost had no changes (**Fig. S3a**). Prolonging the reaction time to 6-8 h, the nanosheets changed into porous nanowalls due to the formation of a large amount of porous NiS (**Fig. 1c** and **Fig. S3b**). However, when the reaction time was extend to more than 10 h (**Fig. S3c** and **3d**), the nanowalls gradually collapsed due to the absence of the inner SnS_2 "skeleton", indicating that SnS_2 was completely transformed into NiS.

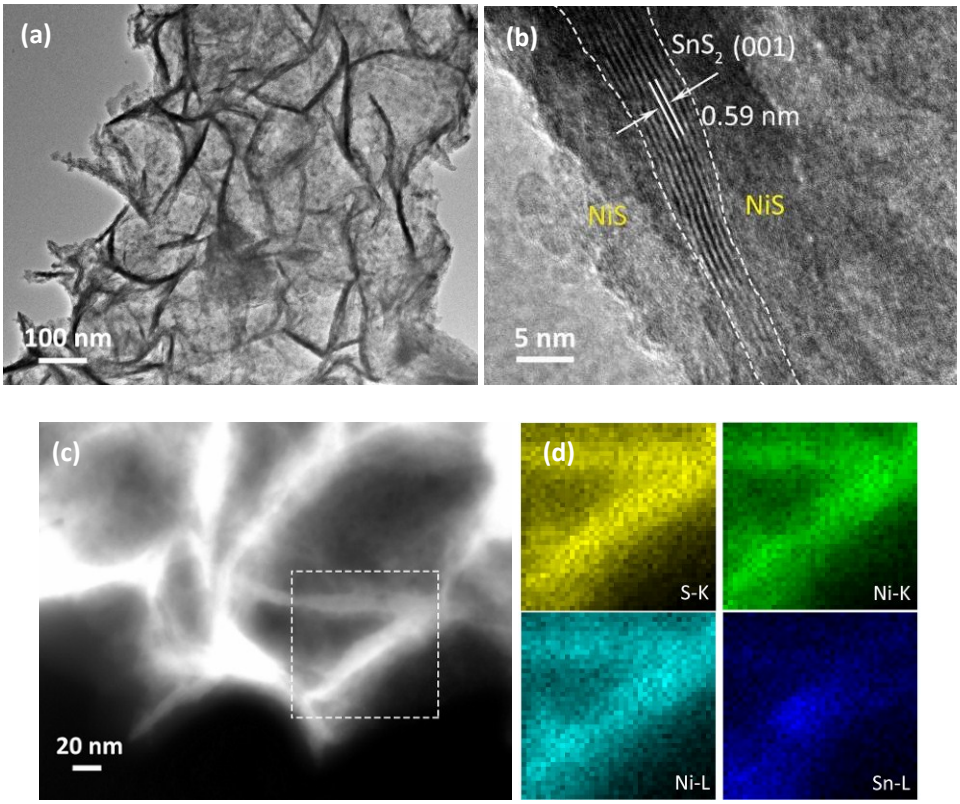

Fig. S4 Typical TEM results for NiS/SnS_2 heterogeneous nanowalls synthesized with a cation-exchange reaction time of 6 h. **(a)** Typical TEM image, **(b)** HRTEM image, **(c)** STEM image, and **(d)** the corresponding elemental mapping images of S, Ni and Sn in the squared area in (c).

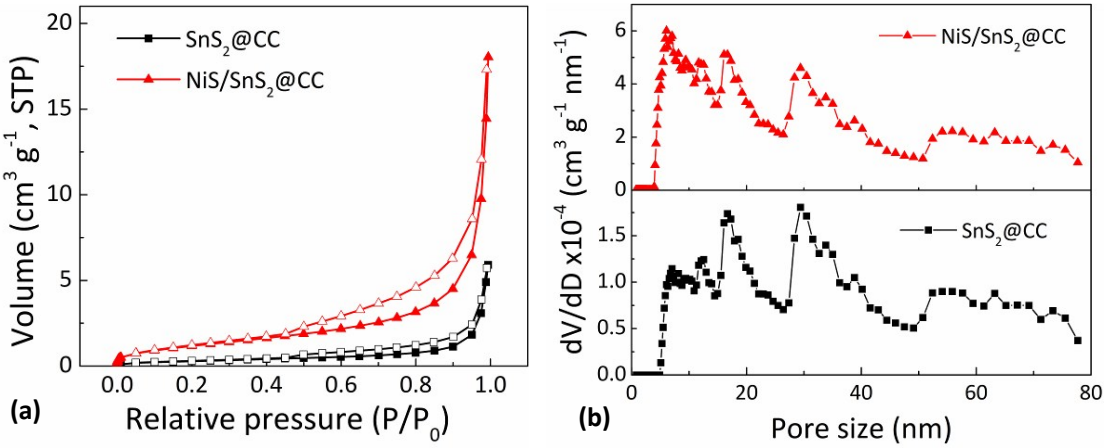

Fig. S5 (a) Nitrogen adsorption/desorption isotherms for the SnS_2@CC and NiS/SnS_2@CC electrodes. **(b)** The corresponding pore-size distribution curves obtained by the BJH method.

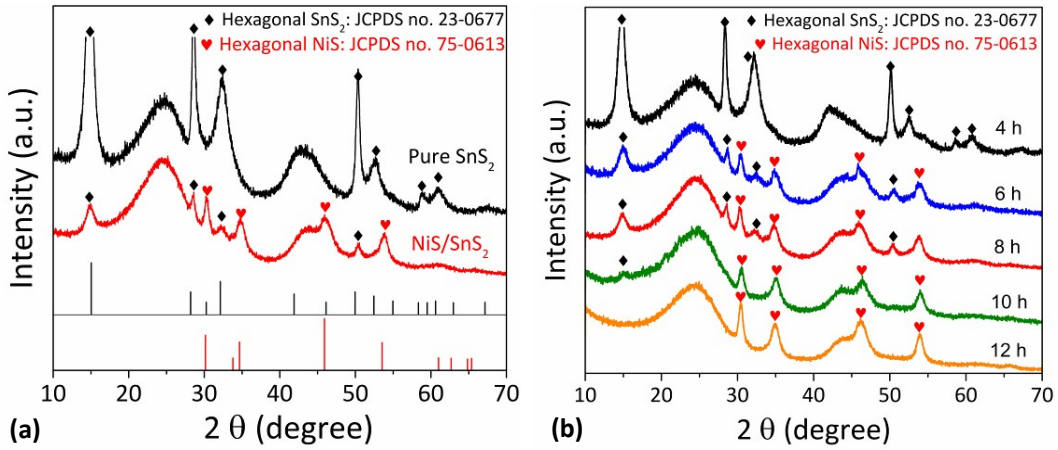

Fig. S6 (a) XRD patterns of SnS_2@CC and NiS/SnS_2@CC (6 h). **(b)** Comparison on the XRD patterns of NiS/SnS_2@CC composites prepared with different cation-exchange reaction times.

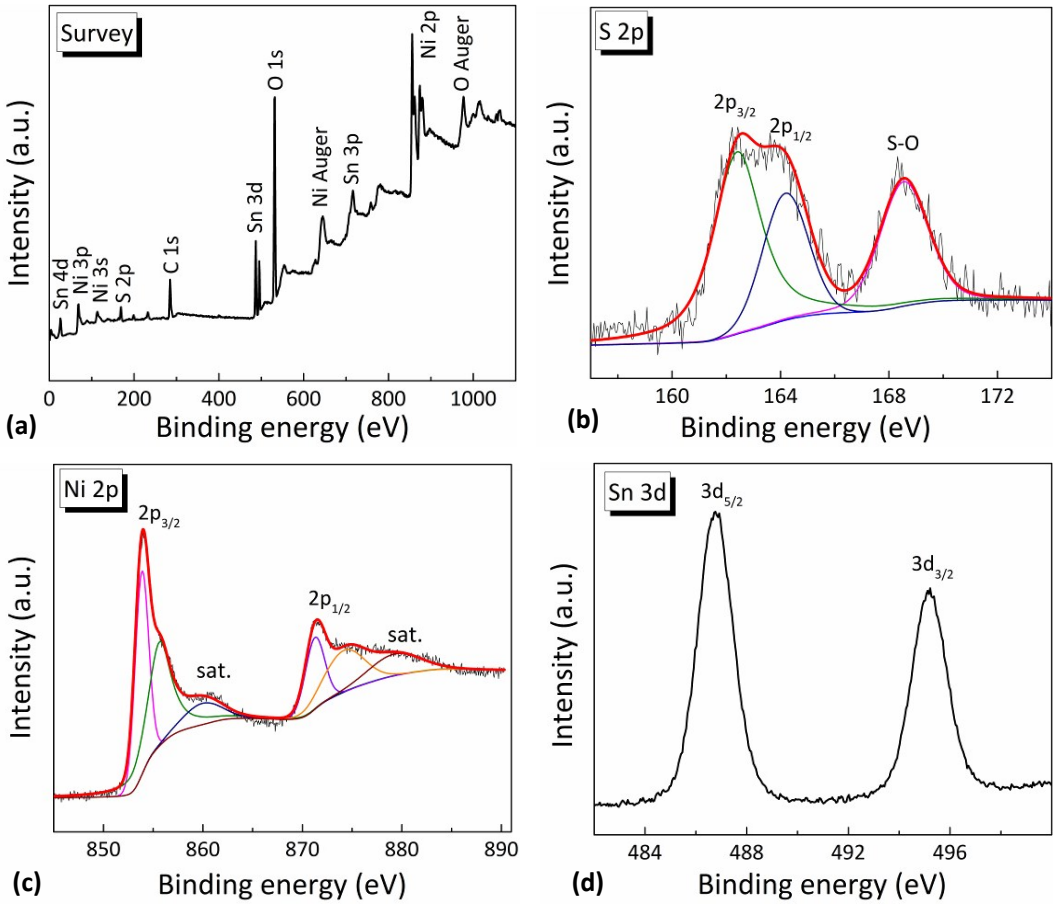

Fig. S7 Typical XPS analysis results for NiS/SnS_2@CC composite (6 h). **(a)** XPS survey spectrum. High-resolution spectra of S 2p **(b)**, Ni 2p **(c)**, and Sn 3d **(d)**.

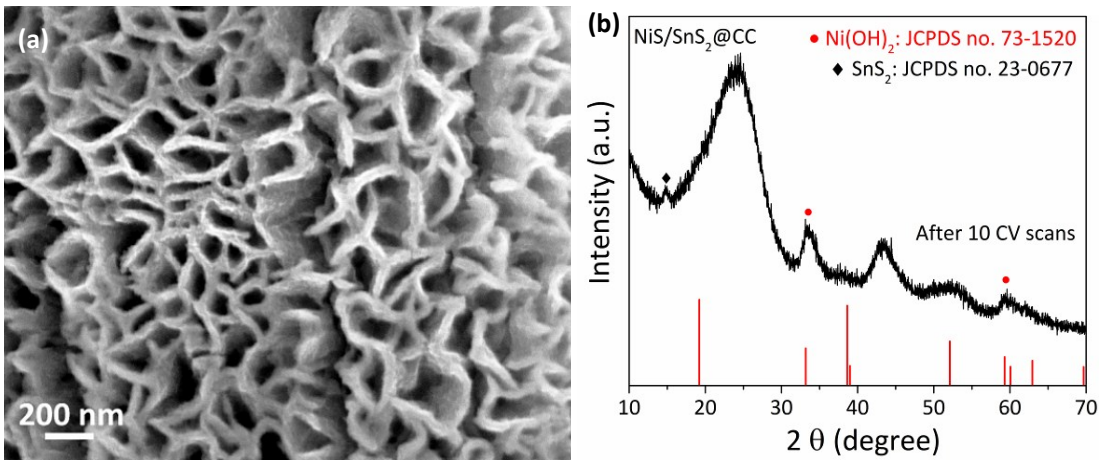

Fig. S8 (a) SEM image and **(b)** XRD pattern of the NiS/SnS_2@CC electrode recorded after the first 10 CV cycles at 2 mV s^{-1}.

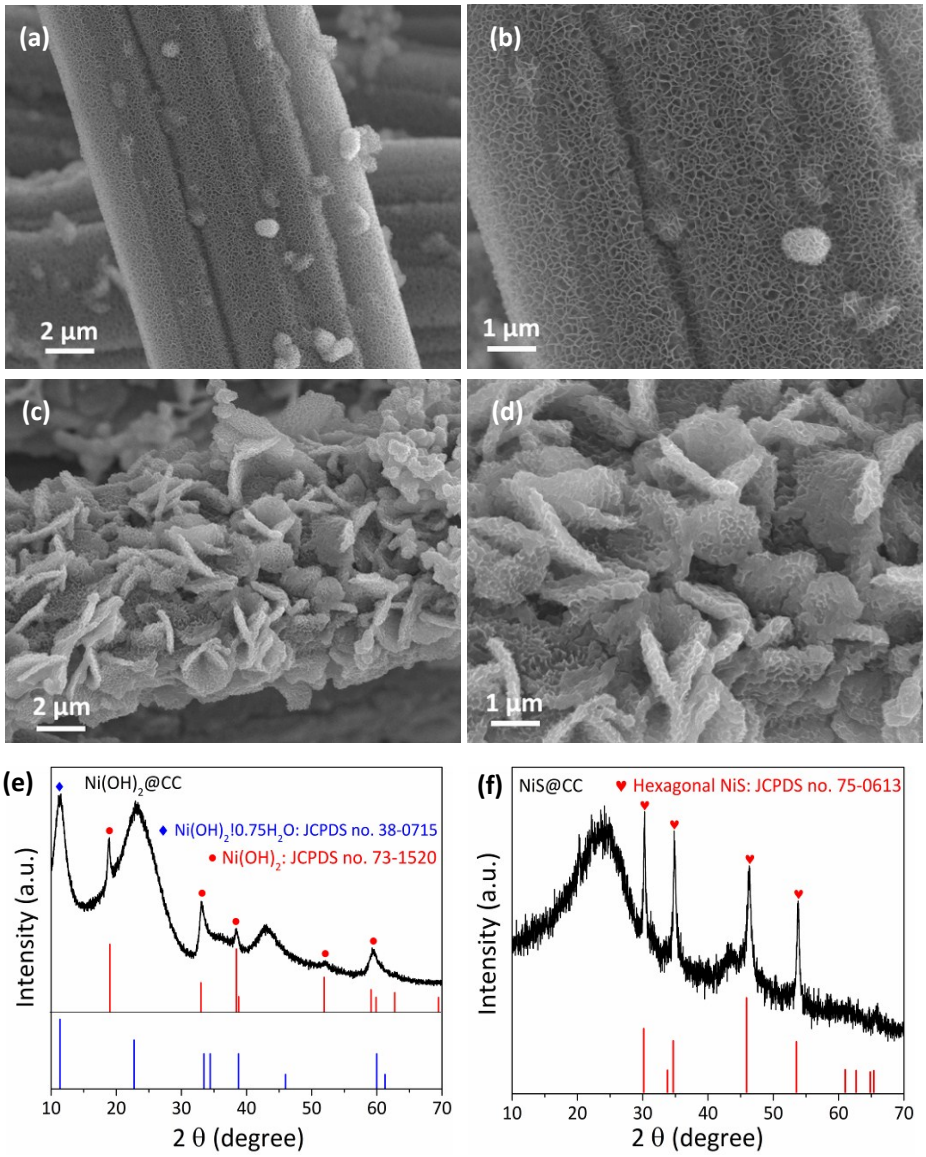

Fig. S9 SEM images at low- and high-magnification of $Ni(OH)_2$@CC **(a,b)** and NiS@CC **(c,d)**. XRD patterns of $Ni(OH)_2$@CC **(e)** and NiS@CC **(f)**.

As shown in **Fig. S9a,b**, many nanosheets vertically covered the surface of carbon fibers to form a honeycomb-like structure. After the sulfidation process, the honeycomb structure re-constructed into many big micro-nanosheets with rough surface (**Fig. S9c,d**). In the XRD pattern of $Ni(OH)_2$@CC (**Fig. S9e**), the peaks marked in red dots match well with the hexagonal $Ni(OH)_2$ phase (JCPDS no. 73-1520). However, the strong and wide peak centered at 2θ value of 11.35˚ can be indexed to the hydrate of rhombohedral $Ni(OH)_2$!$0.75H_2O$ phase (JCPDS no. 38-0715). For the XRD pattern of NiS@CC, all the peaks can be assigned to the hexagonal NiS phase (JCPDS no. 75-0613), which is similar to the XRD result of NiS/SnS_2@CC.

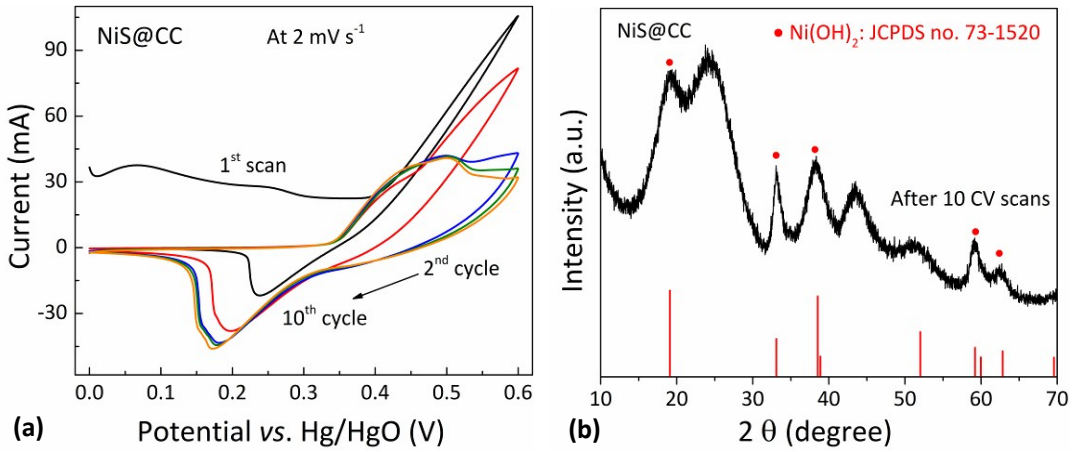

Fig. S10 (a) The first 10 CV cycles at 2 mV s^{-1} for the NiS@CC electrode. **(b)** XRD pattern of NiS@CC recorded after 10 CV cycles.

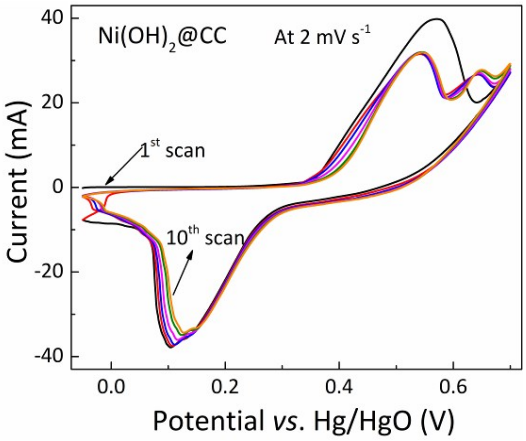

Fig. S11 The first 10 CV cycles at 2 mV s^{-1} for the $Ni(OH)_2$@CC electrode.

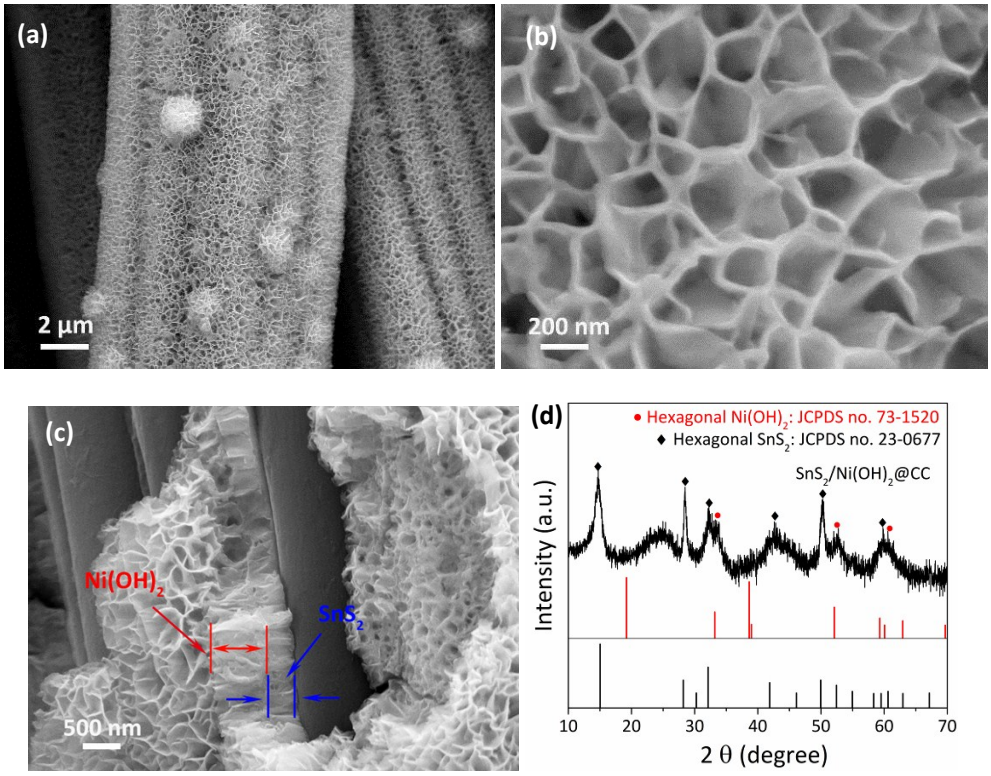

Fig. S12 SEM images **(a-c)** and XRD pattern **(d)** of $Ni(OH)_2/SnS_2$@CC.

To make a fair comparison with NiS/SnS_2@CC, $Ni(OH)_2/SnS_2$@CC was further prepared by growing $Ni(OH)_2$ on the surface of SnS_2@CC. In the SEM images as shown in **Fig. S12a,b**, the $Ni(OH)_2$ nanosheets are wrapped on the surface of SnS_2@CC, and each nanosheet shows an average size of approximately 200 nm and a thickness of about 50 nm. From the SEM image of a fractured surface (**Fig. S12c**), it can be seen that the $Ni(OH)_2$ nanosheets epitaxially grew on the SnS_2 nanosheets template (see **Fig. S1**), and the thickness of the $Ni(OH)_2$ layer is about 700 nm. According to the weight change before and after the $Ni(OH)_2$ growth, the content of $Ni(OH)_2$ was calculated as about 56.4 wt.%.

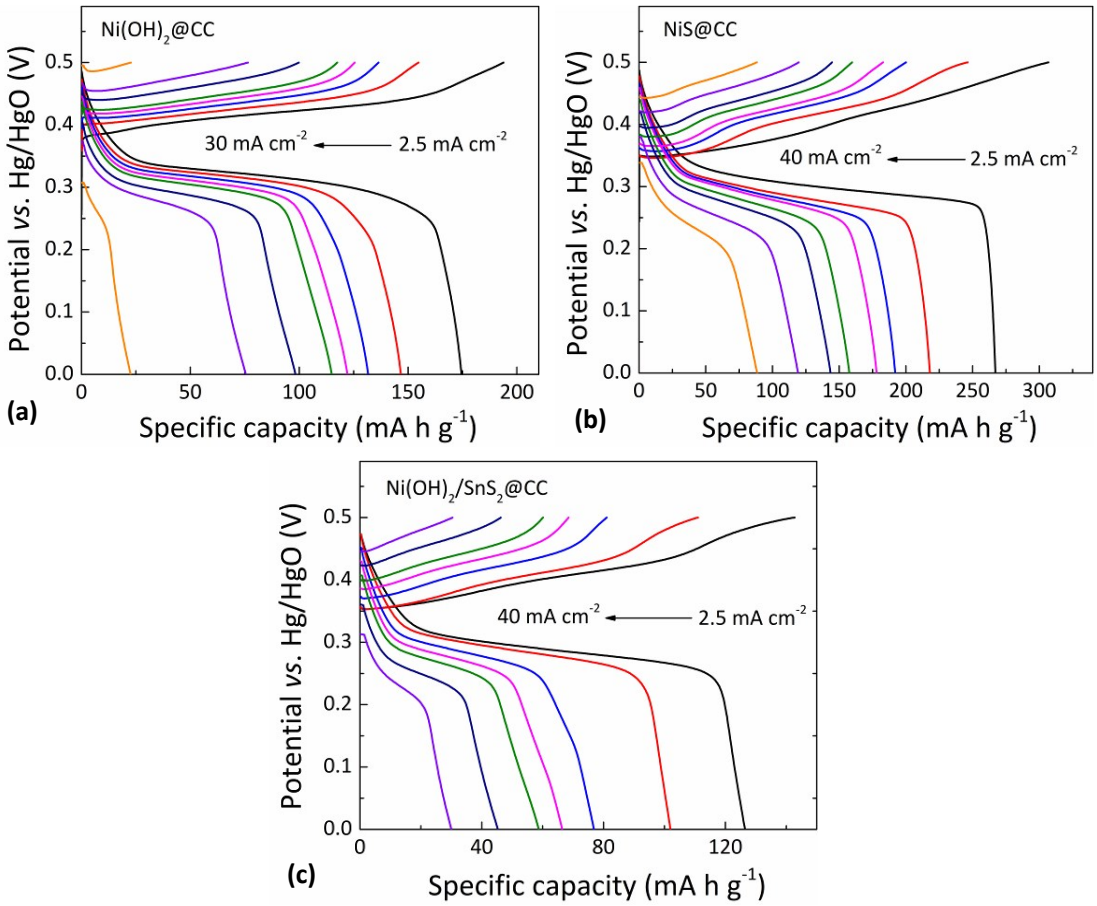

Fig. S13 GCD curves for **(a)** $Ni(OH)_2$@CC, **(b)** NiS@CC and **(c)** $Ni(OH)_2/SnS_2$@CC electrodes at different current densities.

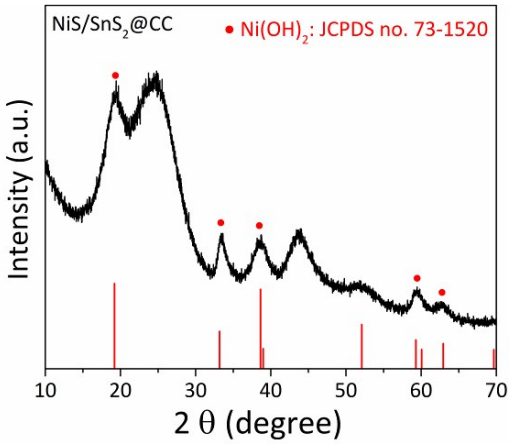

Fig. S14 XRD pattern of the NiS/SnS_2@CC electrode after 1000 GCD cycles at 15 mA cm^{-2}.

For the NiS/SnS_2@CC electrode after 1000 GCD cycles at a high current density of 15 mA cm^{-2}, all the diffraction peaks can be indexed to the $Ni(OH)_2$ phase, indicating that $Ni(OH)_2$ is still the main redox active species in the NiS/SnS_2@CC electrode. However, the peaks for SnS_2 are not detected in XRD pattern, possibly because SnS_2 has changed into amorphous state after a long-time redox reaction.

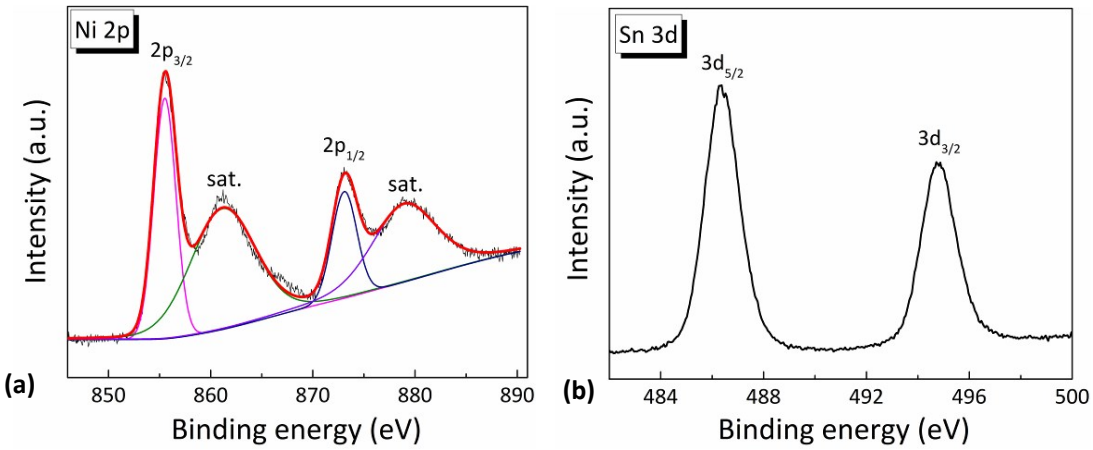

Fig. S15 High-resolution XPS spectra of **(a)** Ni 2p and **(b)** Sn 3d for the NiS/SnS_2@CC electrode after 1000 GCD cycles at 15 mA cm^{-2}.

In Ni 2p high-resolution spectrum (**Fig. S15a**), the peaks at 855.6 and 873.1 eV are matching well with the binding energies of Ni $2p_{3/2}$ and Ni $2p_{1/2}$ for Ni^{2+} in $Ni(OH)_2$, respectively. The two wide peaks at 861.3 and 879.1 eV can be assigned to the corresponding satellite peaks.[S1] For Sn 3d spectrum (**Fig. S15b**), the two distinct peaks at 486.8 and 495.2 eV are well matching with the binding energies of $3d_{5/2}$ and $3d_{3/2}$ for Sn^{4+} in SnS_2, which is consistent with **Fig. S7d**. This result confirms the existence of SnS_2 in NiS/SnS_2@CC electrode after 1000 GCD cycles.

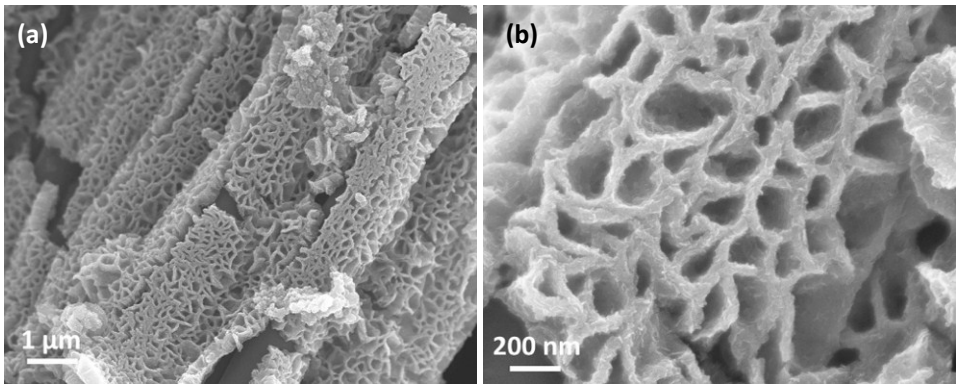

Fig. S16 (a) Low- and **(b)** high-magnification SEM images of the NiS/SnS_2@CC electrode after 1000 GCD cycles at 15 mA cm^{-2}.

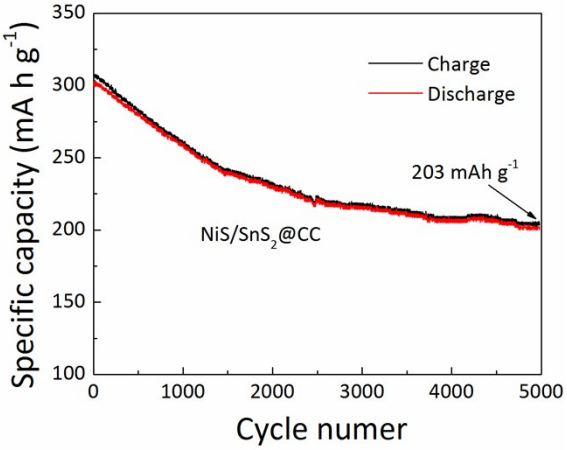

Fig. S17 Long-term GCD testing results of NiS/SnS_2@CC electrode, which were measured at a constant current density of 15 mA cm^{-2}.

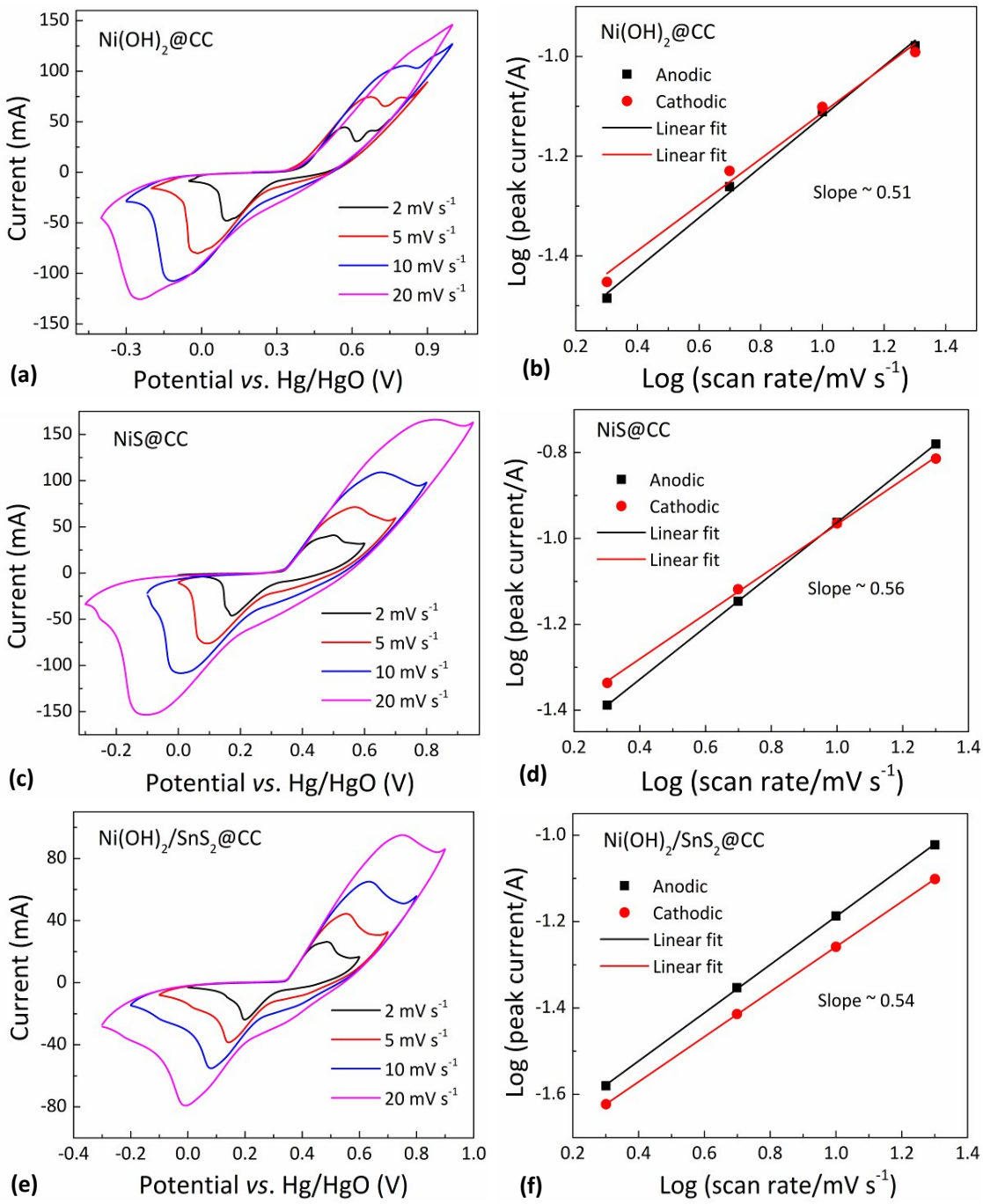

Fig. S18 CV curves at different scan rates and the corresponding linear fittings of the log (peak current) versus log (scan rate) for the cathodic and anodic peaks over **(a,b)** $Ni(OH)_2$@CC, **(c,d)** NiS@CC and **(e,f)** $Ni(OH)_2/SnS_2$@CC electrodes, respectively.

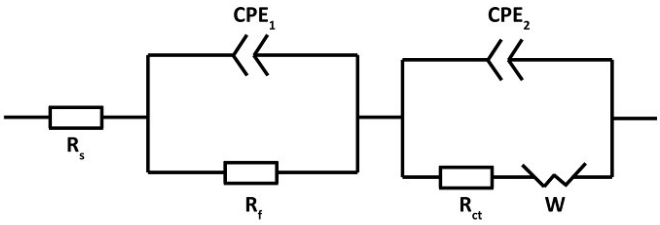

Fig. S19 Equivalent circuit model of the Nyquist diagram for the impedance measurement of the electrodes.

R_s is the inner series resistance of the cell, R_f is the surface film resistance, R_{ct} is the charge transfer resistance, *CPE* is the constant phase element, and *W* is the Warburg diffusion resistance.

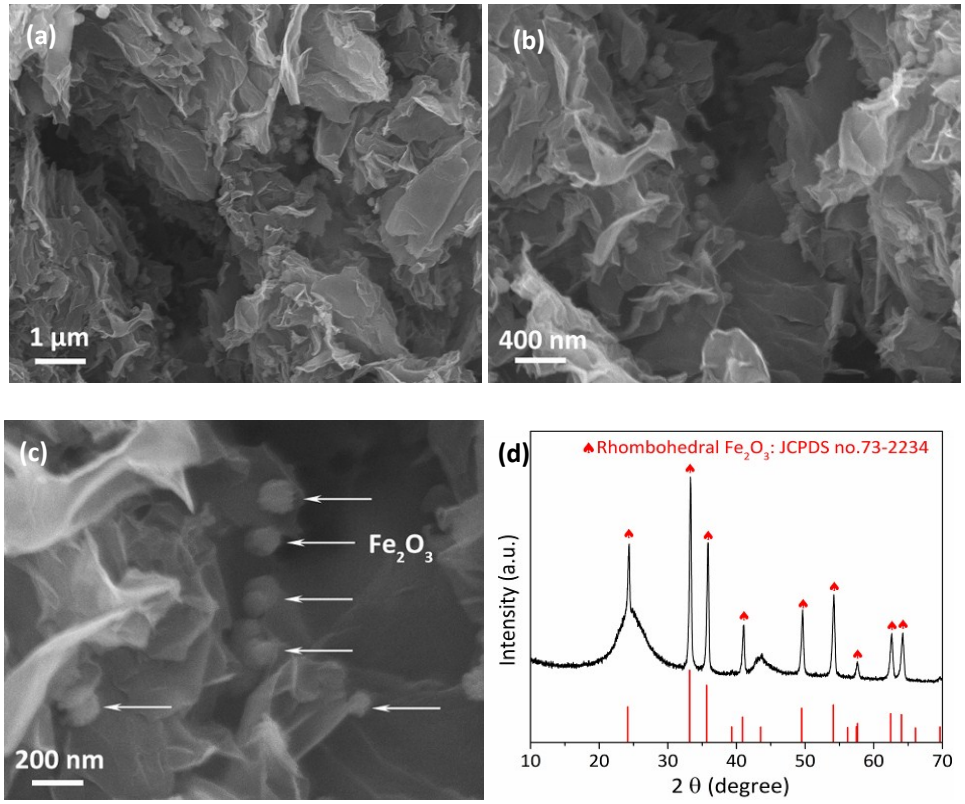

Fig. S20 (a-c) Low- to high-magnification SEM images and **(d)** XRD pattern of the as-prepared Fe_2O_3/rGO nanocomposite.

From **Fig. S20a-c**, it can be seen that many Fe_2O_3 nanoparticles with a diameter of approximately 100 nm are uniformly distributing in the matrix of rGO. As shown in **Fig. S20d**, all the sharp diffraction peaks are matching well with those of the rhombohedral Fe_2O_3 phase (JCPDS no. 73-2234), and the two weak humps centered at 2θ values of 25° and 43° can be indexed to the amorphous carbon species in rGO. All these results confirm that the Fe_2O_3/rGO nanocomposite was successfully synthesized. Moreover, the content of Fe_2O_3 in Fe_2O_3/rGO is about 37.3 wt.%, which is estimated by the weight change before and after the etching of Fe_2O_3.

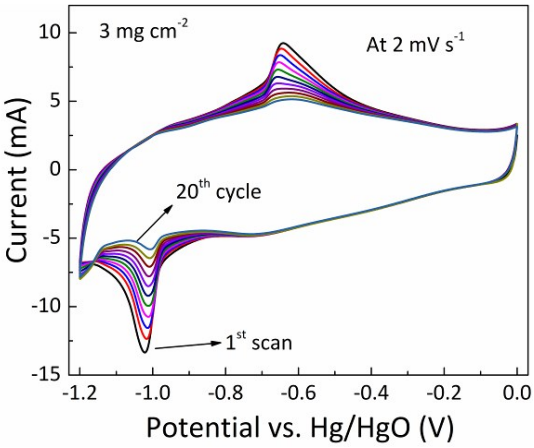

Fig. S21 The first 20 CV cycles at 2 mV s^{-1} for the Fe_2O_3/rGO electrode with a mass loading of 3 mg cm^{-2}.

Similarly, the CV curves change along with the scan time, indicating that there is a phase transformation process over the Fe_2O_3/rGO electrode. According to Ref. S2, such a phase transformation process can be described as follows:

$$Fe_2O_3 + H_2O \rightarrow 2FeOOH \quad (1)$$

Fe_2O_3 changes into low-crystalline FeOOH nanoparticles, which is the active species for the charge-storage in alkaline aqueous solution:

$$FeOOH + H_2O + e^- \leftrightarrow Fe(OH)_2 + OH^- \quad (2)$$

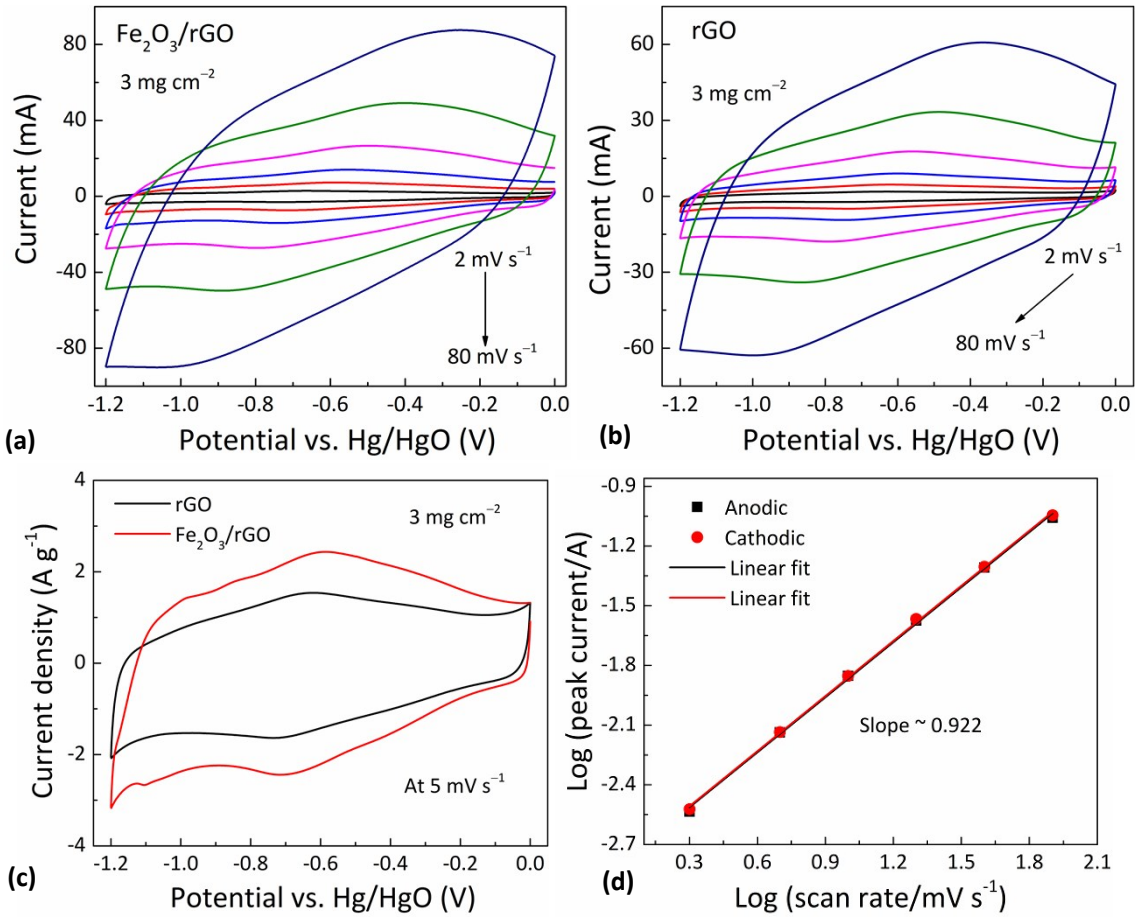

Fig. S22 CV curves at various scan rates from 2 to 80 mV s^{-1} of **(a)** Fe_2O_3/rGO and **(b)** rGO electrode. **(c)** The comparison on CV curves at 5 mV s^{-1} of Fe_2O_3/rGO and rGO electrodes. **(d)** The linear fittings of log (peak current) versus log (scan rate) for the Fe_2O_3/rGO electrode. The loading amounts of the active materials for the Fe_2O_3/rGO and rGO electrodes are both 3 mg cm^{-2}.

As shown in **Fig. S22a**, for the Fe_2O_3/rGO electrode, a pair of wide redox peaks can be observed at all scan rates and their peak position and intensity change with the scan rate. As a comparison, the rGO electrode was prepared by completely etching Fe_2O_3 in the Fe_2O_3/rGO composite. As shown in **Fig. S22b**, the CV curves of the rGO electrode are similar to those of the Fe_2O_3/rGO electrode. Considering the high content of rGO (62.7 wt.%) in the Fe_2O_3/rGO composite, generally the electrochemical performance of Fe_2O_3/rGO electrode is mainly contributed by rGO. However, as is seen from the CV comparison in **Fig. S22c**, the bare rGO electrode shows a lower capacity than the Fe_2O_3/rGO electrode, indicating that combining with Fe_2O_3 could enhance the specific capacity of the anode, because the pseudocapacitive material could store more charges through the redox reaction

process. In addition, from the fitted plot of log (peak current, *i*) and log (scan rate, *v*) for the Fe_2O_3/rGO electrode, it can be seen that β value (0.922) is very close to 1 (**Fig. S22d**), implying that the kinetics of charge storage process for the Fe_2O_3/rGO electrode is mainly controlled by a surface-controlled process and Fe_2O_3/rGO is a pseudocapacitive electrode material.

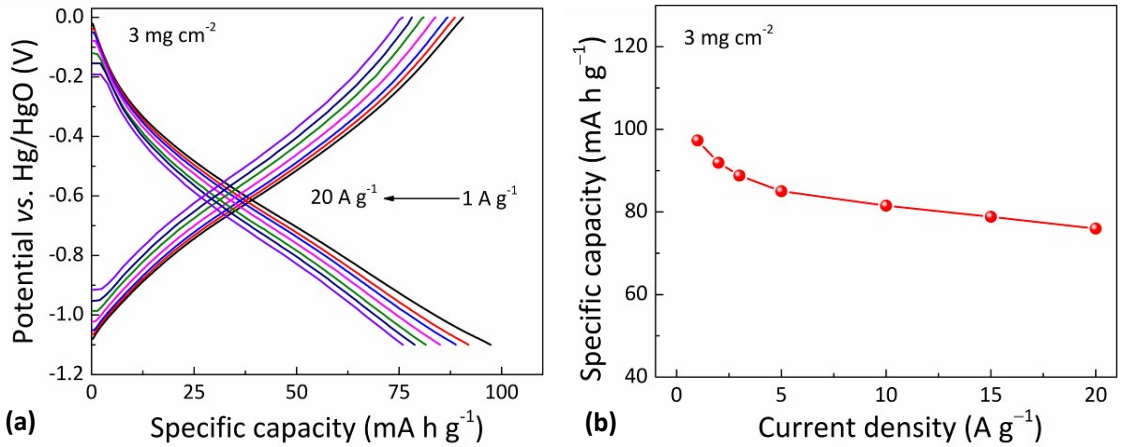

Fig. S23 (a) GCD curves and **(b)** the corresponding specific capacities of the Fe_2O_3/rGO electrode with a mass loading of 3 mg cm^{-2}.

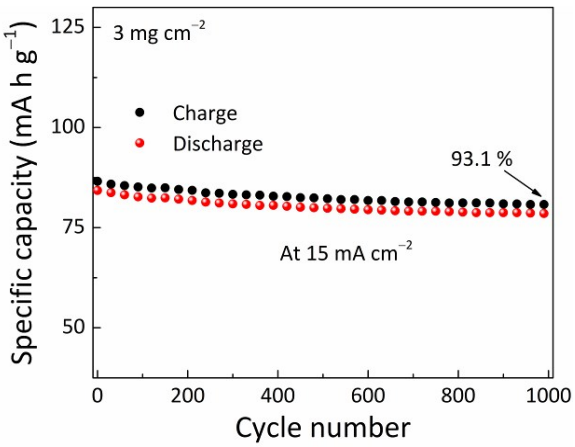

Fig. S24 Cycling stability of the Fe_2O_3/rGO electrode with a mass loading of 3 mg cm^{-2}, which was tested at a current density of 15 mA cm^{-2}.

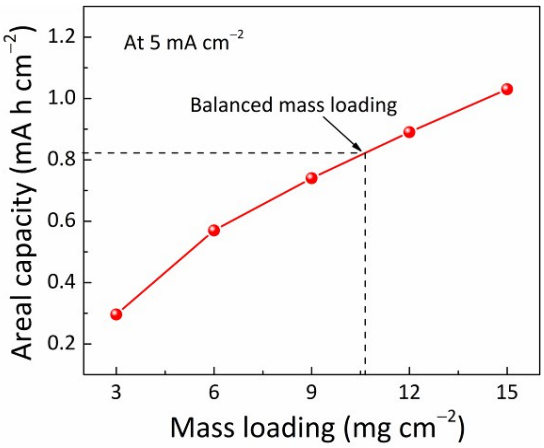

Fig. S25 Areal capacities of the Fe_2O_3/rGO electrode with different mass loadings. All the samples were tested at a current density of 5 mA cm^{-2}.

As shown in **Fig. S25**, the areal capacity (C_a) of the Fe_2O_3/rGO electrode increases with the increases of mass loading. To obtain a balance between the NiS/SnS_2@CC and Fe_2O_3/rGO@CC electrodes, a suitable mass loading for the Fe_2O_3/rGO electrode should be ascertained. Based on the charge balance equation $Q^+ = Q^-$, for complanate electrodes, the areal capacity of a cathode (C_a^+) should equal to that of an anode (C_a^-). According to the result shown in **Fig. 2e** (in Main Text), at a current density of 5 mA cm^{-2}, $C_a^+ = C_s^+ \times m_+ = 0.8163$ mA h cm^{-2}. From the C_a *vs.* m plots (**Fig. S25**), to obtain the C_a value of 0.8163 mA h cm^{-2}, the mass loading should be approximately 10.7 mg cm^{-2} (the intersection of two dash lines). Thus, the balanced mass loading of the Fe_2O_3/rGO electrode is 10.7 mg cm^{-2}.

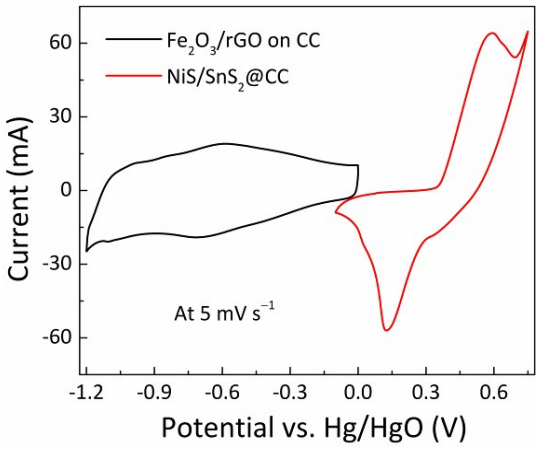

Fig. S26 Comparison on the CV curves of the Fe_2O_3/rGO (m = 10.7 mg cm^{-2}) and NiS/SnS_2@CC electrodes at different potential windows, which were collected at a scan rate of 5 mV s^{-1}.

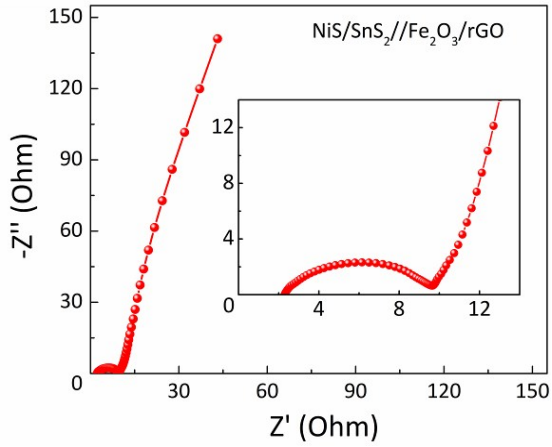

Fig. S27 EIS Nyquist plots of the NiS/SnS_2//Fe_2O_3/rGO BSH device, where the inset shows the enlarged view in the high-frequency range. The R_s is about 2.32 Ω, and R_{ct} is about 7.45 Ω.

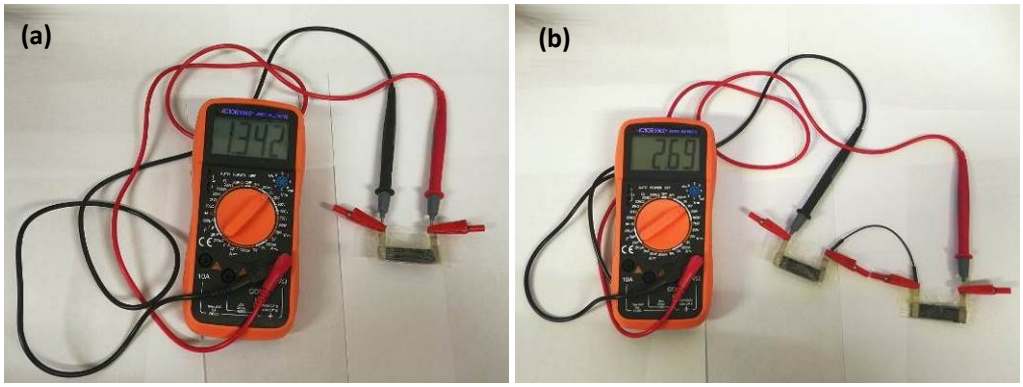

Fig. S28 Optical photographs showing the operation voltages of **(a)** a single cell and **(b)** two tandem $NiS/SnS_2//Fe_2O_3$/rGO BSH devices.

As shown in **Fig. S28**, the operation voltages of a single cell and two tandem $NiS/SnS_2//Fe_2O_3$/rGO BSH devices were measured as 1.342 and 2.69 V, respectively. It should be noted that the practical operation voltage is always lower than the voltage window used for GCD test due to the voltage drop that originates from the internal resistance of the whole circuit.

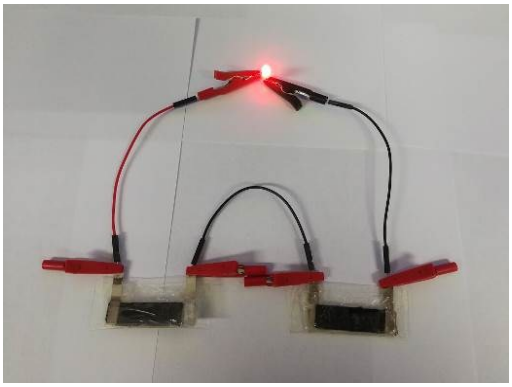

Fig. S29 Optical photograph exhibiting a red LED indicator (1.8 V) powered by two normal tandem $NiS/SnS_2//Fe_2O_3$/rGO BSH devices.

Supplementary Table

Table S1 Comparison on the energy storage performance of our NiS/SnS_2@CC electrode with previously reported high-performance battery-type cathode materials for aqueous electrolytes

Electrode material[a]	Mass loading (mg cm^{-2})	Electrolyte[b]	Specific capability (mA h g^{-1})	Current density	Rate capability	Stability	Ref.
NiS/SnS_2@CC	**2.15**	**6 M KOH**	**430.4**	**2.5 mA cm^{-2} (1.16 A g^{-1})**	**43% (50 mA cm^{-2}) (23.26 A g^{-1})**	**82.6% (1000)**	**This work**
$CoNiO_2$@$Ni(OH)_2$/CNT	1.23	3 M KOH	539.3	1 mA cm^{-2}	69.8% (10 mA cm^{-2})	/	[10]
Cd-Co-Sn nanorods/NF	2.00	2 M KOH	192	1 A g^{-1}	76% (15 A g^{-1})	95.3% (1000)	[11]
Ni-Mo-S nanosheets/NF	1.80	KOH	312	1 mA cm^{-2}	78.8% (50 mA cm^{-2})	96.6% (10000)	[25]
Zn-Co-S nanowires/NF	/	6 M KOH	366.7	3 mA cm^{-2}	62.1% (40 mA cm^{-2})	93.2% (10000)	[35]
Ni-Co-N/$NiCo_2O_4$/graphite fibers	/	3 M KOH	384.8	4 A g^{-1}	86.5% (20 A g^{-1})	99.8% (3000)	[51]
TP-Ni_xS_y/rGO nanoflakes	/	2 M KOH	224.2	1 A g^{-1}	72% (20 A g^{-1})	/	[54]
NiO@CNTs@CuO/Cu fibers	/	1 M KOH	230.48	0.96 mA	76.8% (12 mA)	82.7% (2000)	[56]
H-TiO_2@$Ni(OH)_2$/C fibers	2.00	6 M KOH	306	1 mV s^{-1}	65% (100 mV s^{-1})	/	[57]
$CoNi_2S_4$/graphene aerogel	2.00	6 M KOH	318.3	1 A g^{-1}	44.3% (30 A g^{-1})	95.8% (10000)	[S3]
$CuCo_2S_4$ nanosheet arrays	3.10	2 M KOH	409.2	3 mA cm^{-2}	77.9% (50 mA cm^{-2})	94.2% (10000)	[S4]
$Ni(OH)_2$@NiO-$NiCo_2O_4$ nanosheet arrays	2.05	3 M KOH	326.7	2 A g^{-1}	89.3% (15 A g^{-1})	98.5% (5000)	[S5]
$(Ni,Co)Se_2$/NiCo-LDHs/CC	/	3 M KOH	170	2 A g^{-1}	71% (20 A g^{-1})	89.5% (3000)	[S6]
NiSe/Ni_3S_2/$Ni_{12}P_5$/NF	8.50	3 M KOH	265	5 mA cm^{-2}	69.6% (60 mA cm^{-2})	96% (2000)	[S7]
Co_3O_4/graphene	/	2 M KOH	135.8	1 A g^{-1}	94% (10 A g^{-1})	99.3% (20000)	[S8]
CoO/Co-Cu-S hierarchical nanotubes	2.00	6 M KOH	320	2 A g^{-1}	74% (30 A g^{-1})	96.5% (5000)	[S9]
Co_9S_8/α-MnS@N-C@MoS_2 nanowires	/	2 M KOH	306	1 A g^{-1}	41.2% (10 A g^{-1})	86.9% (10000)	[S10]

[a] C: carbon; CNT: carbon nanotube; NF: nickel foam; LDHs: layered double hydroxides

[b] M: mol L^{-1}

Supplementary Note

Note S1: Calculation of OH^- diffusion coefficient

The solid-state diffusion coefficient of OH^- (D_{OH^-}) in the electrodes can be estimated through the following equations:[S11]

$$D_{OH^-} = \frac{1}{2}\left(\frac{RT}{AF^2n^2C\sigma_\omega}\right)^2 \quad (3)$$

$$Z' = R_s + R_f + R_{ct} + \sigma_\omega\sqrt{\omega} \quad (4)$$

where R denotes the gas constant (8.314 J mol^{-1} K^{-1}), T is the absolute temperature (298.15 K), F is the Faraday constant (96485.33 C mol^{-1}), A is the footprint area of the electrodes (1 cm^2), C is the molar concentration of OH^- in the electrode materials (~0.006 mol cm^{-3}), and σ_ω is the Warburg coefficient. n is the number of electrons per molecule involved in the half-reaction for the redox couple, which can be estimated using **Eq. 8** in the Main Text. Clearly, all the n values of the NiS/SnS_2@CC, $Ni(OH)_2$/SnS_2@CC, NiS@CC, and $Ni(OH)_2$@CC electrodes are 1.

References

S1. Q. Q. Ke, C. Guan, M. R. Zheng, Y. T. Hu, K. H. Ho and J. Wang, *J. Mater. Chem. A*, 2015, **3**, 9538-9542.

S2. K. A. Owusu, L. B. Qu, J. T. Li, Z. Y. Wang, K. N. Zhao, C. Yang, K. M. Hercule, C. Lin, C. W. Shi, Q. L. Wei, L. Zhou and L. Q. Mai, *Nat. Commun.*, 2017, **8** 14267.

S3. G. J. He, M. Qiao, W. Y. Li, Y. Lu, T. T. Zhao, R. J. Zou, B. Li, J. A. Darr, J. Q. Hu, M. M. Titirici and I. P. Parkin, *Adv. Sci.*, 2017, **4** 1600214.

S4. A. Bahaa, J. Balamurugan, N. H. Kim and J. H. Lee, *J. Mater. Chem. A*, 2019, **7**, 8620-8632.

S5. C. V. V. M. Gopi, P. J. S. Rana, R. Padma, R. Vinodh and H. J. Kim, *J. Mater. Chem. A*, 2019, **7**, 6374-6386.

S6. X. Li, H. J. Wu, C. Guan, A. M. Elshahawy, Y. T. Dong, S. J. Pennycook and J. Wang, *Small*, 2019, **15** 1803859.

S7. K. Y. Tao, Y. Gong and J. H. Lin, *Nano Energy*, 2019, **55**, 65-81.

S8. S. H. Yang, Y. Y. Liu, Y. F. Hao, X. P. Yang, W. A. Goddard, X. L. Zhang and B. Q. Cao, *Adv. Sci.*, 2018, **5** 1700659.

S9. W. Lu, J. L. Shen, P. Zhang, Y. J. Zhong, Y. Hu and X. W. D. Lou, *Angew. Chem. Int. Edit.*, 2019, **58** 15441.

S10. S. Kandula, K. R. Shrestha, N. H. Kim and J. H. Lee, *Small*, 2018, **14** 1800291.

S11. K. Kretschmer, B. Sun, J. Q. Zhang, X. Q. Xie, H. Liu and G. X. Wang, *Small*, 2017, **13** 1603318.